The 9th European Congress on Computational Methods in Applied Sciences and Engineering
ECCOMAS Congress 2024
3–7 June 2024, Lisboa, Portugal

CONTINUOUS ADJOINT-BASED OPTIMIZATION OF A HIGH ASPECT-RATIO WING BUSINESS JET IN TRANSITIONAL FLOWS

MARINA G. KONTOU[1], XENOFON S. TROMPOUKIS[1,2], VARVARA G. ASOUTI[1,2] AND KYRIAKOS C. GIANNAKOGLOU[1]

[1]Parallel CFD & Optimization Unit, School of Mechanical Engineering
National Technical University of Athens, Athens, Greece
e-mail: {mkontou,kgianna@mail}.ntua.gr

[2]FOSS: Flow & Optimization, Software & Services, Piraeus, Greece
e-mail: xeftro@gmail.com, vasouti@fossgp.com

Key words: Aerodynamic Shape Optimization, Continuous Adjoint, Transitional Flows, Adjoint to Transition Models, Green Aviation

Summary. This paper contributes to the continuous effort to design wings for aircraft with improved efficiency and reduced environmental footprint. Among others, there is a strong interest in the design of Natural Laminar Flow (NLF) wings by extending the area with laminar flow over them, for reduced drag (and emissions) while ensuring environmental sustainability. The design of NLF wings requires computational tools that can accurately simulate transition from laminar to turbulent flow and the same tools should, also, be incorporated into the optimization loop. In aerodynamic shape optimization, gradient-based algorithms usually rely on the adjoint method to compute gradients, since this is the most cost-effective way to do so. In this work, the continuous adjoint method to the $\gamma - \tilde{R}e_{\theta t}$ transition model, coupled with the Spalart-Allmaras turbulence model is formulated and presented. This is used for the shape optimization of the High Aspect-Ratio Wing of a business jet for minimum drag, subjected to lift and geometrical constraints. The in-house GPU-accelerated PUMA code, which incorporates the primal and adjoint solvers as well as the parameterization tool into a stand-alone tool, is used to carry out the optimization.

1 INTRODUCTION

Air transportation is among the most important segments of the transportation sector and is expected to witness significant growth in the upcoming years. However, this growth is concomitant with increased fuel consumption and increased greenhouse gases. For this reason, the aeronautical sector has taken actions towards environmental sustainability, to meet the goals for affordable and green energy by the year of 2030[1] and climate neutrality by 2050[2]. Relevant research includes methods for the design of Natural Laminar Flow (NLF) wings, [1]. The idea is to extend the area over the wing where the flow is laminar, to reduce drag. To this end, the availability of a computational tool accurately capturing the transitional phenomena with low

[1]https://undocs.org/A/RES/70/1
[2]https://eur-lex.europa.eu/legal-content/EN/TXT/?uri=CELEX:52019DC0640

computational cost is essential. Should this be available, next step is to build the corresponding adjoint solver and incorporate both of them into a gradient-based optimization loop.

In aerodynamic shape optimization, gradient-based methods almost exclusively rely on the adjoint method to compute the gradient of objective functions (J) with respect to (w.r.t.) the design variables b_i, $i=1,\ldots,N$. Its cost is independent of the number of design variables N, being almost equal to that of solving the primal equations. While the differentiation of the turbulence model (in both discrete and continuous adjoint) is nowadays a common approach, [2, 3, 4], the literature regarding the differentiation of transition models is restricted and exclusively related to discrete adjoint, [5, 6, 7]. The first continuous adjoint for transitional flows of compressible fluids was recently developed by the group of authors in [8] for the $\gamma-\tilde{R}e_{\theta t}$ transition model coupled with the Spalart–Allmaras turbulence model. The development was performed for three variants of the $\gamma-\tilde{R}e_{\theta t}$ model, namely the SA-noft2-Gamma-Retheta, [9], the SA-LM2015 and the SA-sLM2015 ones [10]; the first two include min./max. operators and conditional statements while in the latter smooth expressions are used instead. The impact of the "frozen transition" assumption (according to which the adjoint to the transition model is neither formulated nor solved) was investigated in [8] and proved to lead to erroneous Sensitivity Derivatives (SDs). The same studies demonstrated the superiority of the SA-sLM2015 variant, particularly within an optimization loop. In the field of aviation, in [11], a constrained multi-point optimization of the wing of a generic business jet aircraft was carried out; the study aimed to minimize drag at cruise conditions under geometrical and aerodynamic constraints. The aerostructural optimization of the wing of a commercial aircraft, by accounting for restrictions in the overall aircraft design, flutter and powered engine, was performed in [12], while the shape optimization of a supersonic aircraft was carried out in [13]; both based on discrete adjoint. In [14], various turbulence and transition models were differentiated based on the discrete adjoint method and the accuracy of gradients was assessed, among others, in a Falcon jet and a generic tail-less configuration with a high aspect-ratio laminar wing in turbulent and transitional flows.

In this paper, the continuous adjoint method for transitional flows (the exact same software developed in [8]) is used in a real-world shape optimization problem, namely that of a High Aspect-Ratio Wing (HARW) of a business jet. The optimization aims to minimize the drag of the aircraft, subjected to lift and geometrical constraints; the lift coefficient refers to the full aircraft configuration and is computed as the weighted sum of the lift and moment coefficients of the wing-body ones. The rest of the paper is organized as follows: the primal equations for transitional flows of compressible fluids are presented in Sec. 2 and the adjoint equations along with their boundary conditions in Sec. 3. These are implemented in the in–house GPU-enabled primal and adjoint solver PUMA which is briefly presented in Sec. 4 and used for the optimization of the HARW in Sec. 5.

2 PRIMAL PROBLEM

In a 3D Cartesian coordinate system x_k ($k=1,2,3$), the governing equations for the transitional flow of a compressible fluid comprise the mean flow (MF) equations, the one-equation Spalart–Allmaras (SA) turbulence model, [15], the two-equation $\gamma-\tilde{R}e_{\theta t}$ transition model (the SA-sLM2015 variant, [10]) and the Hamilton-Jacobi equation computing the distance field Δ

from the closest solid walls. These are written as

$$R_n^{\mathrm{MF}} = \frac{\partial f_{nk}^{\mathrm{inv}}}{\partial x_k} - \frac{\partial f_{nk}^{\mathrm{vis}}}{\partial x_k} = 0 \quad , \quad n = 1, .., 5 \tag{1a}$$

$$R^{\tilde{\nu}} = \frac{\partial \left(\rho v_k \tilde{\nu}\right)}{\partial x_k} - \frac{\rho}{\sigma}\left\{\frac{\partial}{\partial x_k}\left[\left(\nu+\tilde{\nu}\right)\frac{\partial \tilde{\nu}}{\partial x_k}\right] + c_{b_2}\frac{\partial \tilde{\nu}}{\partial x_k}\frac{\partial \tilde{\nu}}{\partial x_k}\right\} - \tilde{P}_{\tilde{\nu}} + \tilde{D}_{\tilde{\nu}} = 0 \tag{1b}$$

$$R^{\gamma} = \frac{\partial \left(\rho v_k \gamma\right)}{\partial x_k} - \frac{\partial}{\partial x_k}\left[\left(\mu + \frac{\mu_t}{\sigma_f}\right)\frac{\partial \gamma}{\partial x_k}\right] - P_{\gamma} + E_{\gamma} = 0 \tag{1c}$$

$$R^{\tilde{Re}_{\theta t}} = \frac{\partial \left(\rho v_k \tilde{Re}_{\theta t}\right)}{\partial x_k} - \frac{\partial}{\partial x_k}\left[\sigma_{\theta t}\left(\mu+\mu_t\right)\frac{\partial \tilde{Re}_{\theta t}}{\partial x_k}\right] - P_{\theta t} - D_{SCF} = 0 \tag{1d}$$

$$R^{\Delta} = \frac{\partial}{\partial x_k}\left(\Delta\frac{\partial \Delta}{\partial x_k}\right) - \Delta\frac{\partial}{\partial x_k}\left(\frac{\partial \Delta}{\partial x_k}\right) - 1 = 0 \tag{1e}$$

Eq. 1a is solved for the conservative flow variables $\mathbf{U}=[\rho \;\; \rho v_1 \;\; \rho v_2 \;\; \rho v_3 \;\; \rho E]^T$ where ρ is the fluid density, v_k $(k=1,2,3)$ are the Cartesian velocity components and E the total energy per unit mass. In Eq. 1a, f_k^{inv} are the inviscid $f_k^{\mathrm{inv}} = [\rho v_k \;\; \rho v_k v_1 + p\delta_{1k} \;\; \rho v_k v_2 + p\delta_{2k} \;\; \rho v_k v_3 + p\delta_{3k} \;\; \rho v_k h_t]^T$ and f_k^{vis} the viscous fluxes $f_k^{\mathrm{vis}} = [0 \;\; \tau_{1k} \;\; \tau_{2k} \;\; \tau_{3k} \;\; v_\ell \tau_{\ell k} + q_k]^T$. p, h_t stand for the fluid's pressure and total enthalpy and δ_{km} is the Kronecker symbol. $\tau_{km} = (\mu+\mu_t)\left(\frac{\partial v_k}{\partial x_m} + \frac{\partial v_m}{\partial x_k} - \frac{2}{3}\delta_{km}\frac{\partial v_\ell}{\partial x_\ell}\right)$ is the stress tensor, $q_k = \mathcal{C}_p\left(\frac{\mu}{\mathrm{Pr}} + \frac{\mu_t}{\mathrm{Pr_t}}\right)\frac{\partial T}{\partial x_k}$ is the heat flux, where μ, μ_t is the molecular and turbulent viscosity, respectively. Pr, Pr_t stand for the Prandtl and turbulent Prandtl numbers and C_p is the fluid's specific heat capacity at constant pressure.

Eq. 1b is solved for $\rho\tilde{\nu}$, where $\tilde{\nu}$ is the turbulence model variable and turbulent viscosity is computed by $\mu_t = \rho\tilde{\nu} f_{v_1}$. The source terms of the SA model, modified to account for transitional phenomena, read

$$\tilde{P}_{\tilde{\nu}} = \gamma\rho c_{b_1}\tilde{S}\tilde{\nu}, \quad \tilde{D}_{\tilde{\nu}} = \rho c_{w_1} f_w \left(\frac{\tilde{\nu}}{\Delta}\right)^2 \tag{2}$$

Eqs. 1c and 1d are solved for $\rho\gamma$ and $\rho\tilde{Re}_{\theta t}$, respectively, where γ is the intermittency and $\tilde{Re}_{\theta t}$ the transition momentum-thickness Reynolds number. The production and destruction terms in the γ and $\tilde{Re}_{\theta t}$ equations read

$$P_\gamma = \rho c_{\alpha_1} F_{length} F_{onset} \phi_{\text{-}300}\left(\zeta, \zeta_{thres}\right)\sqrt{\gamma}\left(1 - c_{e_1}\gamma\right), E_\gamma = \rho c_{\alpha_2} F_{turb} \phi_{\text{-}300}\left(\zeta, \zeta_{thres}\right)\gamma\left(c_{e_2}\gamma - 1\right) \tag{3}$$

$$P_{\theta t} = \rho\frac{c_{\theta t}}{\mathcal{T}}\left(Re_{\theta t}^{eq} - \tilde{Re}_{\theta t}\right)\left(1 - F_{\theta t}\right), D_{SCF} = c_{\theta t}\frac{\rho}{\mathcal{T}} c_{cf}\phi_{\text{-}300}\left[\left(Re_{SCF} - \tilde{Re}_{\theta t}, 0\right)\right] F_{\theta t} \tag{4}$$

Undefined terms/constants for the turbulence and transition models can be found in [15, 10].

Along the adiabatic solid walls, the no-slip condition $v_k = 0$ is imposed, while for the turbulence and transition variables $\tilde{\nu} = 0$, $\frac{\partial \gamma}{\partial n} = 0$ and $\frac{\partial \tilde{Re}_{\theta t}}{\partial n} = 0$. The far-field boundary is treated as a synthesis of inflow and outflow boundaries, depending on the local velocity direction. At the inflow boundaries, four flow quantities are imposed as Dirichlet conditions and one is extrapolated from the interior. There is an opposite treatment along the outflow boundaries, with one flow quantity kept fixed and the rest being extrapolated from the domain interior. For the SA model, the viscosity ratio $\left(\frac{\nu_t}{\nu}\right)_\infty$ is defined along the far-field boundary, while γ_∞=1 and $\tilde{Re}_{\theta t,\infty}$ is computed as in [10].

3 ADJOINT PROBLEM

This study deals with three objective/constraint functions J, namely the drag (J_1), lift (J_2) and pitching moment (J_3) coefficients of the aircraft. These are expressed as

$$J_{1,2}=\frac{F}{\frac{1}{2}\rho_\infty U_\infty A_{\text{ref}}},\quad F=\int\limits_{S_{\text{W}}}(p\mathsf{n}_k-\tau_{km}\mathsf{n}_m)\,r_k dS$$

$$J_3=\frac{T_Y}{\frac{1}{2}\rho_\infty U_\infty A_{\text{ref}} l_{\text{ref}}},\quad T_Y=\int\limits_{S_{\text{W}}}\epsilon_{2lk}\,(p\mathsf{n}_k-\tau_{km}\mathsf{n}_m)\left(x_l-x_l^{\text{ref}}\right)dS$$

where F stands for the aerodynamic force acting on the aircraft in the direction defined by r_k. For $r_k=(\cos\alpha_\infty,\sin\alpha_\infty)$, F stands for drag; for $r_k=(-\sin\alpha_\infty,\cos\alpha_\infty)$, F is aircraft's lift. T_Y is the pitching moment (in the application studies of this paper, the spanwise direction is along the y-axis) computed w.r.t. to reference point x^{ref}. ρ_∞, U_∞, α_∞ are the free-stream fluid density, velocity magnitude and the angle of attack, respectively, while A_{ref}, l_{ref} stand for the reference surface and length, and ϵ_{ijk} is the Levi-Civita symbol.

In continuous adjoint, J is augmented by the field integrals of the products of the governing equations' residuals with the adjoint variable fields, resulting in the augmented function J_{aug}. Differentiating this w.r.t. b_i yields

$$\frac{\delta J_{\text{aug}}}{\delta b_i}=\frac{\delta J}{\delta b_i}+\int\limits_\Omega\left(\Psi_n\frac{\delta R_n}{\delta b_i}+\tilde{\nu_a}\frac{\delta R^{\tilde{\nu}}}{\delta b_i}+\gamma_a\frac{\delta R^{\gamma}}{\delta b_i}+\tilde{Re}_a\frac{\delta R^{\tilde{Re}_{\theta t}}}{\delta b_i}+\Delta_a\frac{\delta R^{\Delta}}{\delta b_i}\right)\mathrm{d}\Omega \tag{5}$$

where $\Psi_n,(n=1,...,5)$ are the adjoint mean flow variables and $\tilde{\nu_a}$, γ_a, $\tilde{Re}_a$ and Δ_a are the adjoint of $\tilde{\nu}$, γ, $\tilde{Re}_{\theta t}$ and Δ, respectively. The adjoint variables act as extra degrees of freedom to avoid computing the derivatives of the primal fields w.r.t. b_i; this is achieved by formulating, discretizing and numerically solving the adjoint PDEs. Upon convergence of the primal equations, $J_{\text{aug}}\equiv J$ and, consequently, $\frac{\delta J}{\delta b_i}\equiv\frac{\delta J_{\text{aug}}}{\delta b_i}$.

Eliminating all volume integrals including derivatives of $\mathbf{U}$, $\rho\tilde{\nu}$, $\rho\gamma$, $\rho\tilde{Re}_{\theta t}$ and Δ w.r.t. b_i leads to the adjoint mean flow, Spalart-Allmaras, transition model and Hamilton-Jacobi equations, written in the following synoptic form:

$$R_m^{\Psi}=-A_{nmk}\frac{\partial\Psi_n}{\partial x_k}-\mathcal{K}_m^{\text{MF}}+\mathcal{K}_m^{\text{SA}}+\mathcal{K}_m^{\gamma\text{–}\tilde{Re}_{\theta t}}=0 \tag{6a}$$

$$R^{\tilde{\nu_a}}=-v_k\frac{\partial\tilde{\nu}_a}{\partial x_k}+\mathcal{G}^{\text{SA,diff}}+\mathcal{G}^{\text{SA,src}}+\mathcal{G}^{\mu_t,\text{MF}}+\mathcal{G}^{\mu_t,\gamma\text{–}\tilde{Re}_{\theta t}}=0 \tag{6b}$$

$$R^{\gamma_a}=-v_k\frac{\partial\gamma_a}{\partial x_k}+\mathcal{H}^{\gamma\text{–}\tilde{Re}_{\theta t},\text{diff}}+\mathcal{H}^{\gamma\text{–}\tilde{Re}_{\theta t},\text{src}}+\mathcal{H}^{\text{SA,src}}=0 \tag{6c}$$

$$R^{\tilde{Re}_a}=-v_k\frac{\partial\tilde{Re}_a}{\partial x_k}+\mathcal{N}^{\gamma\text{–}\tilde{Re}_{\theta t},\text{diff}}+\mathcal{N}^{\gamma\text{–}\tilde{Re}_{\theta t},\text{src}}+\mathcal{N}^{\text{SA,src}}=0 \tag{6d}$$

$$R^{\Delta_a}=-2\frac{\partial}{\partial x_k}\left(\Delta_a\frac{\partial\Delta}{\partial x_k}\right)+\mathcal{M}^{\text{SA,src}}+\mathcal{M}^{\gamma\text{–}\tilde{Re}_{\theta t},\text{src}}=0 \tag{6e}$$

with $n=1,\ldots,5$, $m=1,\ldots,5$ and $k=1,\ldots,3$. $\mathcal{K}$, $\mathcal{G}$, $\mathcal{H}$, $\mathcal{N}$ and $\mathcal{M}$ result from the differentiation of the flow equations w.r.t. U, $\rho\tilde{\nu}$, $\rho\gamma$, $\rho\tilde{Re}_{\theta t}$ and Δ, respectively, with superscripts specifying the corresponding term in the differentiated equations. Their full expressions can be found in [8].

Since Eqs. 6a-6d do not depend on Δ_a, Eq. 6e is numerically solved after them as it contributes to the SDs.

In a similar manner, the elimination of the surface integrals that contain derivatives of the flow variables w.r.t. b_i leads to the adjoint boundary conditions. Namely, along the adiabatic walls (S_W), the adjoint no-slip condition reads $\Psi_{m+1} = \frac{\partial J}{\partial(\tau_{km}\mathsf{n}_k)}$, the adjoint adiabatic condition is $q_k^{\text{adj}}\mathsf{n}_k = 0$, while $\tilde{\nu_a} = 0$, $\frac{\partial \gamma_a}{\partial x_k}\mathsf{n}_k = 0$ and $\frac{\partial \tilde{Re}_a}{\partial x_k}\mathsf{n}_k = 0$. Along the far-field boundaries (S_{F}), the derivatives of shear stress and heat flux w.r.t. b_i can be neglected. Let V_λ^{loc} be the flow quantities extrapolated from the interior of the domain (for subsonic inflow boundaries 1 Riemann variable is extrapolated, while 4 variables are extrapolated over the subsonic outflow boundaries), then $\Psi_n A_{nmk}\mathsf{n}_k \frac{\partial U_m}{\partial V_\lambda^{\text{loc}}} = 0$. Moreover, $\tilde{\nu}_{a,\infty} = 0$, $\gamma_{a,\infty} = 0$, $\tilde{Re}_{a,\infty} = 0$ and $\Delta_{a,\infty} = 0$.

After satisfying the field adjoint equations and their boundary conditions, the remaining field and surface integrals comprise the formula for computing the gradient of J w.r.t. b_i. Details about the expression of the SDs can be found in [8].

4 THE PUMA SOFTWARE

All computations were performed using the NTUA in-house GPU-accelerated flow and adjoint solver, PUMA [16]. PUMA solves the primal and adjoint equations on unstructured/hybrid grids using vertex-centered finite volumes. PUMA runs on a GPU cluster and employs either the MPI protocol for data communications between GPUs on different computing nodes or the shared on-node memory for transactions between GPUs on the same node. High parallel efficiency is achieved by the use of Mixed Precision Arithmetics (MPA), [16], as this reduces the memory footprint of the code and transactions of the GPU threads with the device, without jeopardizing code's accuracy. In particular, all L.H.S. operators are computed with double precision but stored in single precision accuracy. On the other hand, the R.H.S. is computed and stored in double precision. Over and above to the primal and adjoint solver, PUMA includes a set of shape parameterization tools and grid morphers based on volumetric Non-Uniform Rational B-Splines (NURBS).

The continuous adjoint code employs consistent discretization schemes recently developed under the name of the *Think-Discrete Do-Continuous* (*TDDC*) adjoint, [17]. This bridges the gap between discrete and continuous adjoint by combining the best of both worlds. The *TDDC* adjoint enjoys the ease of implementation, the physical insight, the low computational cost and memory footprint of continuous adjoint, with the accuracy of SDs computed by discrete adjoint, without an excessive memory footprint, though. The *TDDC* adjoint discretization schemes for turbulent/transitional flows are presented, in detail, in a companion ECCOMAS paper (Kontou et al, *Consistent Discretization Schemes for the Continuous Adjoint Equations in Aerodynamic Shape Optimization for Turbulent/Transitional Flows*).

5 SHAPE OPTIMIZATION OF A HARW BUSINESS JET MODEL

The geometry of a HARW business jet model (wing-body configuration) and the cruise conditions were provided by Dassault Aviation in the framework of the NEXTAIR project (*multi-disciplinary digital-enablers for NEXT-generation AIRcraft design and operations*) funded by the European Union under Grant Agreement No. 101056732. The optimization of the HARW model aimed at minimizing C_D, with constant $C_L = 0.50$, where C_L refers to the full configura-

tion model (that includes, also, the horizontal tail plane and the powered engine), approximated as the weighted sum of lift and pitching moment coefficients computed at the wing-body configuration. Hereafter, C_L denotes the lift coefficient of the full configuration.

Prior to the optimization, the flow around the baseline business jet was simulated. The study was performed for three different Mach numbers, $M_\infty = 0.76$, 0.78 and 0.80 and four angles of attack (AoA $\in [0°, 1°, 2°, 3°]$). The Reynolds number and turbulence intensity level were common in all cases, namely, $Re = 4.24 \cdot 10^6$ and $Tu = 0.1\,\%$. A hybrid unstructured CFD grid of $\sim 12.4M$ nodes was generated around half of the aircraft, with $y^+ < 0.7$ for the first nodes off the wall. The computed polar diagrams, using the standard SA model and the SA-sLM2015 model are presented in Fig. 1. For all Mach numbers, the use of the transition model shifted the polar diagram to smaller C_D values (around ~ 20 drag counts) with a slight increase in C_L. The pressure (C_p) and skin friction (C_f) fields on the wing-body surface are presented in Fig. 2 for the upper side of the aircraft, for $M_\infty = 0.78$ and AoA $= 2°$. The top-half of this figure corresponds to a simulation performed without, while the bottom-half, with transition model. The C_p and C_f distributions on different cuts of the wing, along the spanwise direction, are also presented in Fig. 3. The use of the transition model moved the location of the shock wave downstream compared to a fully turbulent simulation, Figs. 2-left and 3-top. Differences between fully turbulent and transitional results are pronounced in the C_f fields, Figs. 2-middle and 3-bottom, as only the use of the transition model can capture the laminar area close to the leading edge; this can also be seen in the intermittency field (γ), Fig. 2-right, where low values of γ indicate the laminar zone.

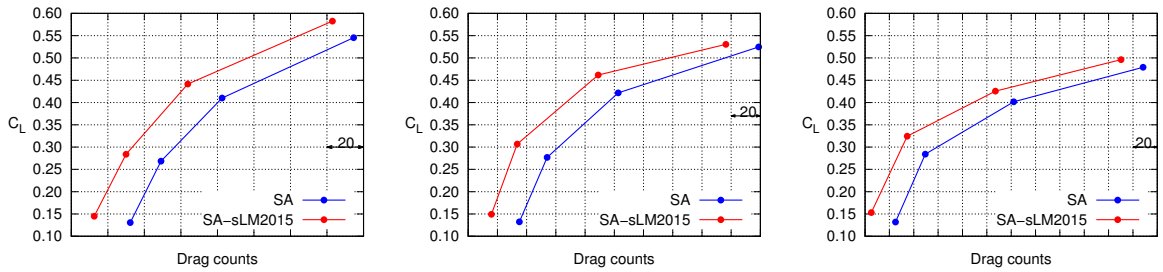

Figure 1: Polar diagram C_L vs. C_D resulted by the SA (no transition model) and the SA-sLM2015 transition model for $M_\infty = 0.76$ (left), $M_\infty = 0.78$ (middle) and $M_\infty = 0.80$ (right). Drag values on the horizontal axis are omitted on purpose. Horizontal spacing corresponds to 20 drag counts.

For the optimization, the wing was parameterized using the 4×9×2 control box of Fig. 4. The control points in red were allowed to move in the normal-to-the-chord (z) direction, in pairs; in specific, every pair of control points sharing the same x and y coordinates could be displaced in the z direction, by retaining the distance between them. Such a way of displacement ensures constant wing thickness distribution and frozen planform during the optimization. Control points in blue remained fixed. In total, 24 design variables were used for the wing optimization.

The optimization was performed for $M_\infty = 0.78$, in two steps. In the first step, the AoA meeting the C_L constraint ($C_L = 0.50$, for the full configuration) was computed. Then, the wing shape optimization followed and the desired C_L value was imposed as constraint. Two optimization runs were performed; the first was based exclusively on the SA turbulence model (without transition model neither in the primal nor the adjoint solver), while the second relied

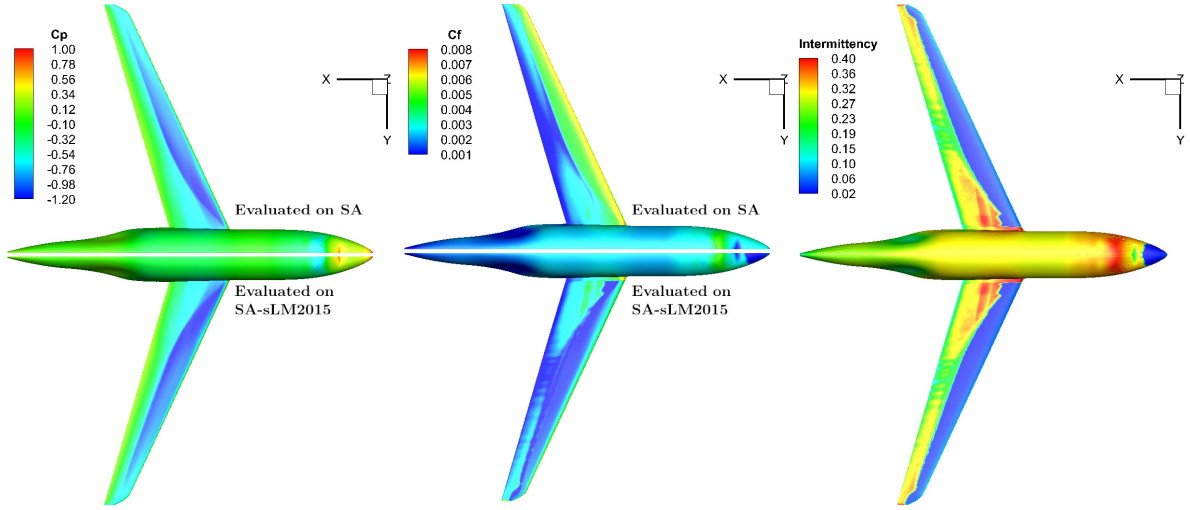

Figure 2: Pressure (C_p, left) and skin friction coefficient (C_f, middle) fields on the aircraft surface for $M_\infty = 0.78$ and AoA $= 2°$. Computations based on the SA without (top-half) and with (bottom-half) the SA-sLM2015 transition model are simultaneously presented. Right: intermittency (γ) field on the aircraft surface computed using the SA-sLM2015 model.

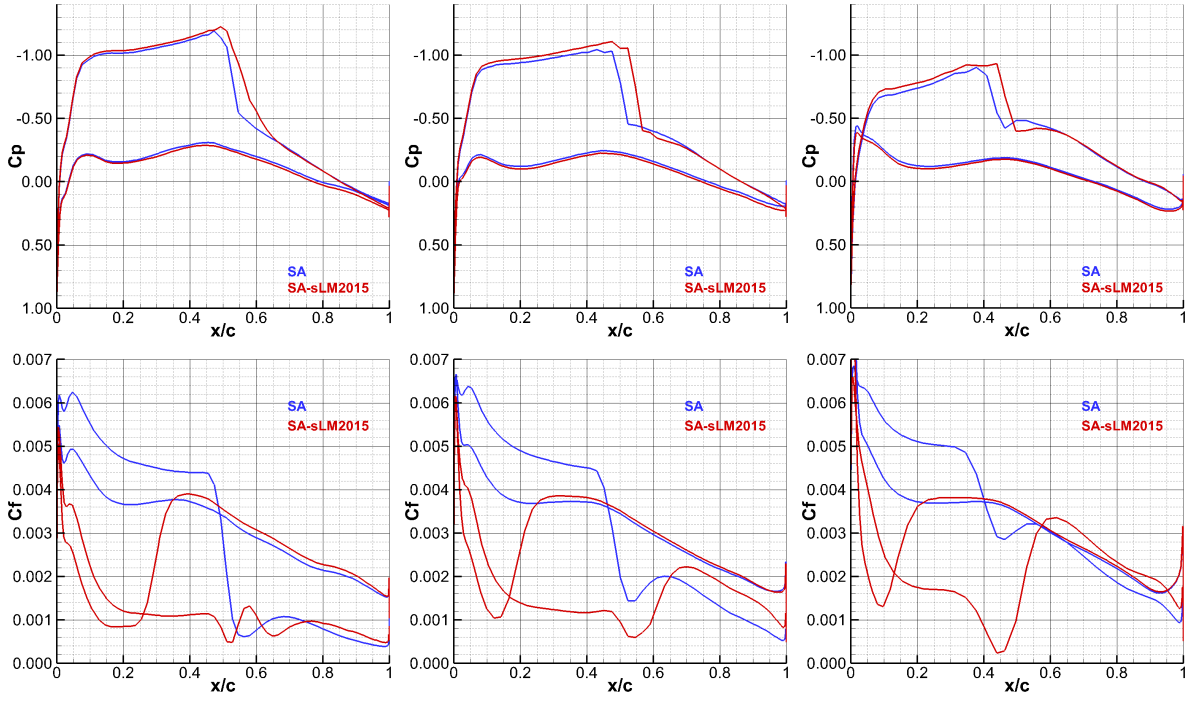

Figure 3: Pressure (C_p, top) and skin friction (C_f, bottom) coefficient distribution on the wing surface at different spanwise cross-sections ($\eta = 0.40$, 0.65, 0.90, from left to right) for $M_\infty = 0.78$ and AoA $= 2°$. Computations based on the SA without (blue) and with the SA-sLM2015 (red) transition model. Abscissa is normalized using the local chord at this spanwise position.

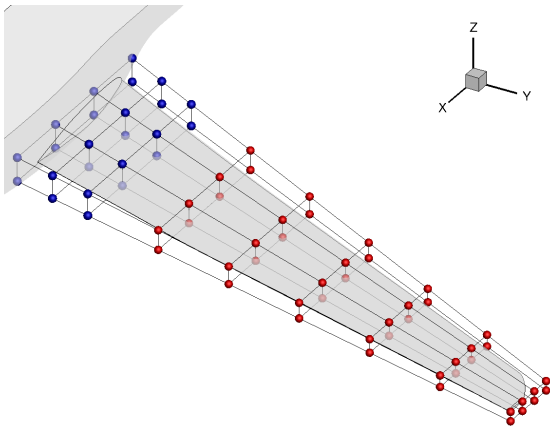

Figure 4: NURBS control lattice set around the wing. Control points in blue are fixed whereas the red are allowed to move in pairs (for the same x and y position) along the z-direction. The wing planform remains constant during the optimization.

on the SA-sLM2015 transition model. These resulted in 17.2% (AoA = 2.67°) and 16.5% (AoA = 2.33°) reduction in the C_D value, respectively, satisfying the C_L constraint, Fig. 5.

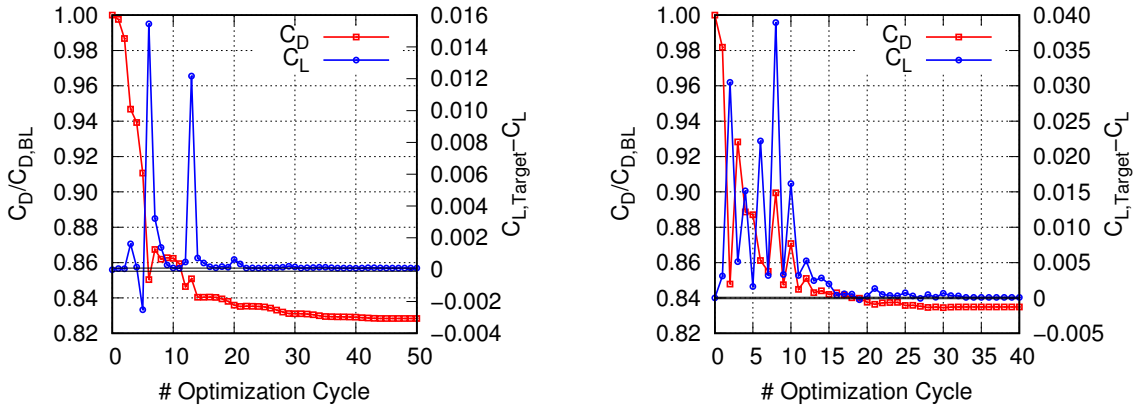

Figure 5: Evolution of the objective (C_D) and constraint (C_L) functions during the optimizations for $M_\infty = 0.78$ and $C_L = 0.5$. Optimization based on the SA turbulence model without transition effects (left) and on the SA-sLM2015 transition model (right). Each optimization cycle comprises one primal and two adjoint (for C_D and C_L) problem solutions.

The difference in the per face C_D between the baseline and the optimized geometries ($\Delta C_D = C_D^{\text{Opt}} - C_D^{\text{BL}}$) is presented in Fig. 6 for the upper and lower sides of the two optimized aircraft. The blue color indicates a decrease, while the red an increase in C_D w.r.t. the baseline configuration. In both optimized shapes, C_D reduction was mostly associated with the area close to the shock wave, especially on the wing suction side. Though there are areas where the per face C_D was increased compared to the baseline geometry (plotted in red), the overall difference of summed up facial contributions led to a high decrease in C_D, in both geometries. The aircraft which was optimized using only the SA model was re-evaluated using the transition model and, as expected,

the C_L constraint was violated. In order to meet the $C_L = 0.5$ constraint and, thus make a fair comparison, a post-hoc optimization by tuning the AoA was performed. This resulted in 15.0% reduction in C_D which is less than the 16.5% reduction achieved with the SA-sLM2015-based optimization. This showcases the importance of including transitional phenomena into the optimization loop.

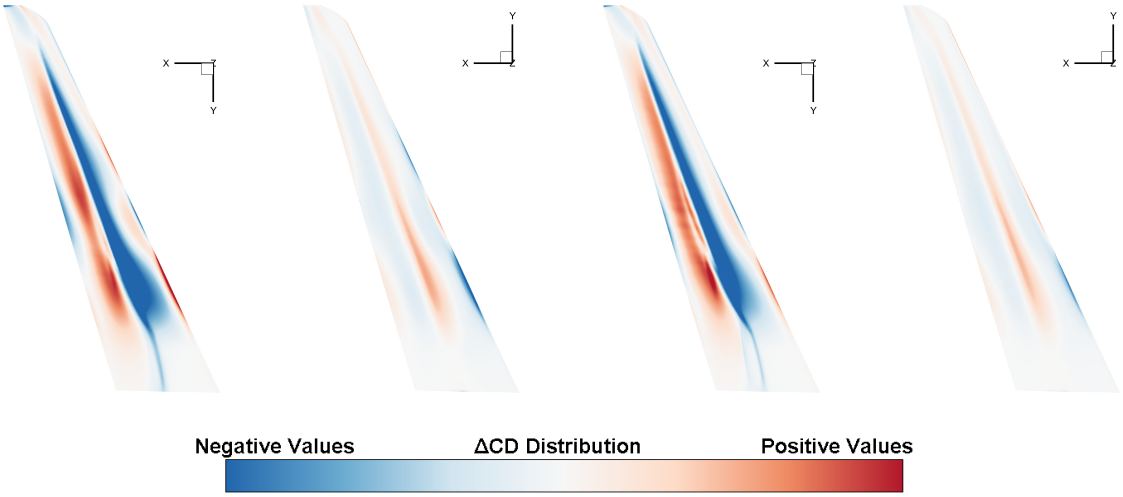

Figure 6: Difference of per face C_D between the baseline and the optimized wings ($\Delta C_D = C_D^{\text{Opt}} - C_D^{\text{BL}}$) as computed based on the SA turbulence (first two) and the SA-sLM2015 transition (last two) model.

The C_p distribution on different spanwise locations are shown in Fig. 7 for the baseline and the two optimized aircraft (all evaluated on the SA-sLM2015 model having $C_L = 0.5$). It can be seen that the location of the shock wave has moved upstream close to wing root and tip, and downstream elsewhere. It is interesting to note that, on the baseline geometry, 66% of C_D was due to pressure forces (pressure drag coefficient, C_{D_p}), with the remaining 34% being due to shear forces (friction drag coefficient, C_{D_f}). The two optimizations decreased C_{D_p} by 25.6% and 27.5%, respectively, while C_{D_f} was slightly increased by 5.4% and 4.8%, respectively. This is why, though not presented herein, the location of the transition line practically remained intact or moved upstream since this is strongly related to C_{D_f} (see Fig. 3).

The effect of transition model into the optimization loop was additionally assessed by comparing the polar diagrams of the full configurations for $M_\infty = 0.78$ of the baseline and the optimized wings. This is presented in Fig. 8 in which the black, blue and red curves correspond to the baseline, optimized with the SA turbulence model and optimized with the SA-sLM2015 transition model aircraft, respectively, all of them evaluated with transition model. The polar diagram for the aircraft geometry optimized using the SA-sLM2015 model (red) is shifted to lower C_D values compared to that optimized without a transition model with re-evaluation on the SA-sLM2015 model (blue), Fig. 8-left. This gain is quantified by the area painted in light blue which exists over the entire length of the polar diagram. However, the polar diagram for the optimized aircraft is shifted to higher C_D values compared to the baseline ones for $C_L < 0.42$ (light red area) and lower C_D values for $C_L > 0.42$ (light blue area), Fig. 8-right. This is confirmed in both optimizations and was expected as single-point optimizations, subjected to constraints on the lift, were carried out.

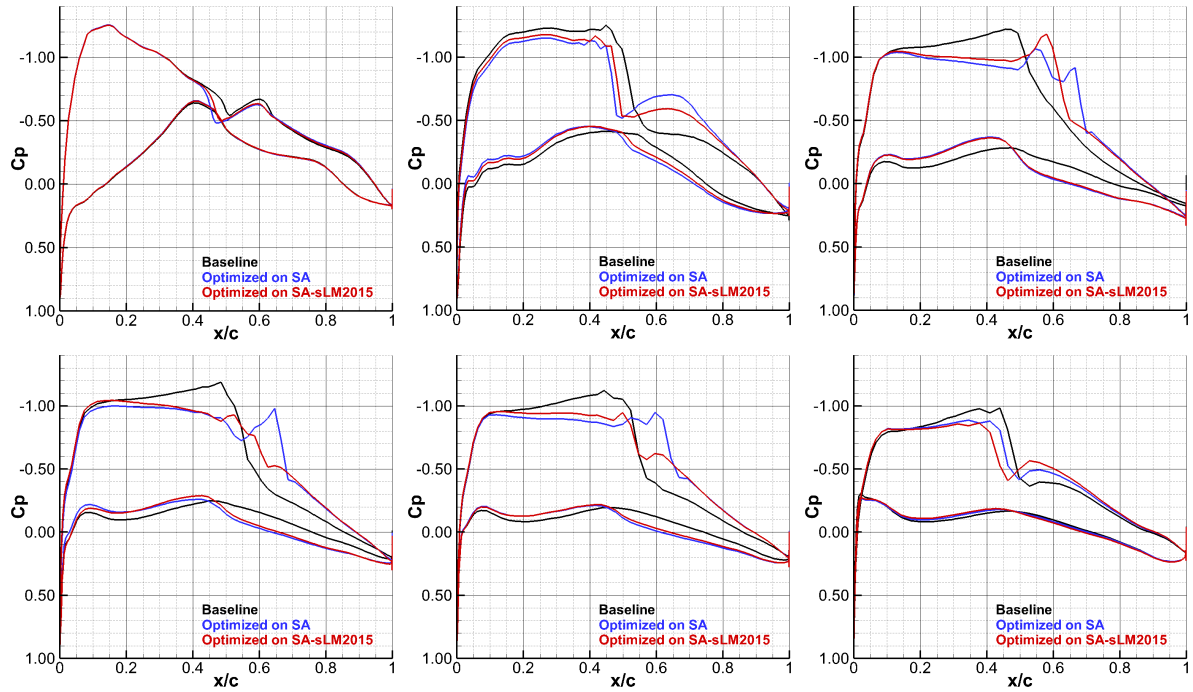

Figure 7: Pressure coefficient (C_p) distribution on the wing surface at different spanwise cross-sections ($\eta = 0.06$, 0.22, 0.40, 0.56, 0.72, 0.90, from top-left to bottom-right) for $C_L = 0.50$ for the baseline (black), optimized with the SA (blue) and the SA-sLM2015 (red) models. All aircraft geometries are evaluated on the SA-sLM2015 transition model. Abscissa is normalized using the local chord at this spanwise position.

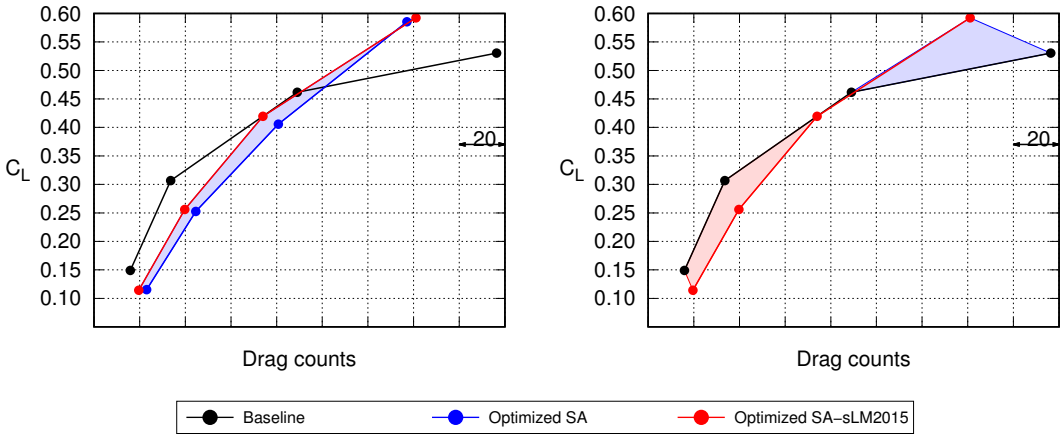

Figure 8: Left: Comparison of the polar curves for $M_\infty = 0.78$ and AoA $= [0°, 1°, 2°, 3°]$ for the baseline (black) and the optimized without (blue) and with the SA-sLM2015 transition model (red) aircraft geometries. The light blue area quantifies the C_D reduction due to the use of transition model into the optimization loop, in the entire range of the polar curve. Right: Comparison between the polar curves of the baseline and the optimized, on the SA-sLM2015 model, aircraft geometry. Light blue and light red regions correspond to the decrease and increase in C_D. All aircraft are (re-)evaluated on the SA-sLM2015 transition model.

6 CONCLUSIONS

In this paper, the continuous adjoint method for transitional flow of compressible fluids was applied in a real-world problem, that of a High Aspect-Ratio Wing business jet shape optimization. The continuous adjoint has been presented for the $\gamma-\tilde{Re}_{\theta t}$ (SA-sLM2015 variant) transition model coupled with the Spalart–Allmaras turbulence model. In the framework of green aviation, the optimization aimed to reduce the drag of the aircraft without damaging lift and also keeping the planform with frozen; deformations were allowed only on the wing camber. In order to quantify the impact of including the transition model into the optimization loop, the optimization was performed twice. The first optimization was based on the SA turbulence model (in both the primal and the adjoint solver) followed by a post-hoc tuning of the AoA (to meet the C_L constraint) using the SA-sLM2015 transition model. The second optimization relied on the SA-sLM2015 transition model. It was demonstrated that including transition into the optimization loop was, indeed, beneficial as it led to a higher decrease in C_D (16.5% compared to 15.0%). Moreover, it was shown that the aircraft optimized using the SA-sLM2015 model and its adjoint has an improved aerodynamic performance than the SA-based one (both evaluated on the transition model), as it resulted to lower C_D values along the entire length of the polar curve and not only at the point the optimization was performed. This is a clear indication that the use of a transition model into the optimization loop is absolutely necessary to accurately capture the transitional phenomena and correctly guide the optimization.

ACKNOWLEDGMENT

This work is part of the NEXTAIR project funded by the European Union under Grant Agreement No. 101056732. The views and opinions expressed are, however, those of the author(s) only and do not necessarily reflect those of the European Union or REA. Neither the European Union nor the REA can be held responsible for them.

REFERENCES

[1] M. Malik, J. Crouch, W. Saric, J. Lin, and E. Whalen. *Application of drag reduction techniques to transport aircraft*, pages 1–10. John Wiley & Sons, Ltd, 2015.

[2] A. Zymaris, D. Papadimitriou, K. Giannakoglou, and C. Othmer. Continuous adjoint approach to the Spalart-Allmaras turbulence model for incompressible flows. *Comput. Fluids*, 38:1528–1538, 2009.

[3] S. Kim, J. Alonso, and A. Jameson. Two-dimensional high-lift aerodynamic optimization using the continuous adjoint method. *AIAAA Paper 2000-4741, 8th Symposium on Multidisciplinary Analysis and Optimization*, 2000.

[4] A. Stück. An adjoint view on flux consistency and strong wall boundary conditions to the Navier–Stokes equations. *J. Comput. Phys.*, 301:247–264, 2015.

[5] P. Khayatzadeh and S. Nadarajah. Aerodynamic shape optimization via discrete viscous adjoint equations for the k–ω SST turbulence and $\gamma - \tilde{Re}_\theta$ transition models. *AIAA Paper 2011-1247, 49th AIAA Aerospace Sciences Meeting including the New Horizons Forum and Aerospace Exposition*, 2011.

[6] G. Halila, J. Martins, and K. Fidkowski. Adjoint-based aerodynamic shape optimization including transition to turbulence effects. *Aerosp. Sci. Technol.*, 107:106243, 2020.

[7] M. Piotrowski and D. Zingg. Investigation of a smooth local correlation-based transition model in a discrete-adjoint aerodynamic shape optimization algorithm. *AIAA Paper 2022-1865, AIAA SCITECH 2022 Forum*, 2022.

[8] M. Kontou, X. Trompoukis, V. Asouti, and K. Giannakoglou. The continuous adjoint method to the $\gamma-\tilde{Re}_{\theta t}$ transition model coupled with the Spalart-Allmaras model for compressible flows. *Int. J. Numer. Methods Fluids*, https://doi.org/10.1002/fld.5319.

[9] V. D'Alessandro, S. Montelpare, R. Ricci, and A. Zoppi. Numerical modeling of the flow over wind turbine airfoils by means of Spalart-Allmaras local correlation based transition model. *Energy*, 130:402–419, 2017.

[10] M. Piotrowski and D. Zingg. Smooth local correlation-based transition model for the Spalart-Allmaras turbulence model. *AIAA J.*, 59:474–492, 2021.

[11] B. Epstein and S. Peigin. Efficient approach for multipoint aerodynamic wing design of business jet aircraft. *AIAA J.*, 45:2612–2621, 2007.

[12] M. Abu-Zurayk, A. Merle, C. Ilic, S. Keye, S. Goertz, M. Schulze, Th. Klimmek, C. Kaiser, D. Quero, J. Häßy, R. Becker, B. Fröhler, and J. Hartmann. Sensitivity-based multifidelity multidisciplinary optimization of a powered aircraft subject to a comprehensive set of loads. In *AIAA AVIATION 2020 FORUM*, 06 2020.

[13] F. Alauzet, S. Borel-Sandou, L. Daumas, A. Dervieux, Q. Dinh, S. Kleinveld, A. Loseille, Y. Mesri, and G. Roge. Multimodel design strategies applied to sonic boom reduction. *European Journal of Computational Mechanics/Revue Européenne de Mécanique Numérique*, 17, 05 2012.

[14] L. Martin, N. Forestier, L. Colo, F. Billard, F. Chalot, Z. Johan, and M. Mallet. Extension of linearized cfd methods for complex aerodynamic flows and application to unsteady load evaluations. In *International Forum on Aeroelasticity and Structural Dynamics IFASD 2022*, 2022.

[15] P. Spalart and S. Allmaras. A one-equation turbulence model for aerodynamic flows. *AIAA J.*, 439:5–21, 1992.

[16] V. Asouti, X. Trompoukis, I. Kampolis, and K. Giannakoglou. Unsteady CFD computations using vertex-centered finite volumes for unstructured grids on Graphics Processing Units. *Int. J. Numer. Methods Fluids*, 67:232–246, 2011.

[17] M. Kontou, X. Trompoukis, V. Asouti, and K. Giannakoglou. On the discretization of the continuous adjoint to the Euler equations in shape optimization. In *ADMOS 2023, International Conference on Adaptive Modeling and Simulation*, Gothenburg, Sweden, 2023.